

Fundamental Examination of Multiple Potential Passive Component Technologies for Future Power Electronics

Phyo Aung Kyaw, *Student Member, IEEE*, Aaron L.F. Stein, and Charles R. Sullivan, *Fellow, IEEE*

Abstract—Efficient and compact high-power high-frequency passive energy storage components are required for miniaturization of power converters, and remain a challenging obstacle in power electronics. In this work, multiple energy storage mechanisms are analyzed on an order-of-magnitude basis to identify potential alternatives for conventional passive components, especially magnetics, which have frequency-dependent power losses. The high energy density of mechanical storage methods provides an attractive alternative to the widely-used LC resonance. Piezoelectric transduction is explored and the performance of a piezoelectric resonator is compared to that of an LC resonator in terms of efficiency and power handling capabilities in a resonant switched-capacitor type circuit. The analysis provides a basis for exploring potential passive energy storage component technologies and comparing their performance limits with those of electromagnetic passive components. The analysis shows that both electromagnetic and mechanical resonance, in the ideal scenarios, can offer much better performance than do passive component technologies in use today. A prototype resonator is built with off-the-shelf C0G capacitors to confirm the low loss and high power predicted by the model. The resulting resonator has an effective resistance of 2.76 m Ω at 2.70 MHz in 1 cm³ volume and can handle 7.42 kW within the rated temperature.

Index Terms—energy storage, piezoelectricity, resonators, resonant power conversion, switched capacitor circuits

I. INTRODUCTION

Switching power converters require passive components, such as inductors, transformers and capacitors, which often dominate the size and loss of power converters. Recent advances in wide-bandgap semiconductors such as GaN and SiC allow for efficient high-frequency power conversion [1], and further improvement to power semiconductor technology may be expected. The major limitations impeding further improvement of power converter density are the densities and power losses of passive components, especially magnetics [2], [3]. Although incremental improvements in magnetics are enabling advances in power density, the importance of the problem merits consideration of the fundamental performance limits of passive components and exploration of possible alternative technologies.

Recent research activities focus on improving magnetics technology for the MHz frequency range, including optimization of inductor geometries and nanoengineering of magnetic materials [4]. Because passive components are used for

storing electrical energy on the time scale of the switching frequency, other energy storage mechanisms may be used as alternatives to the magnetic and electrostatic passives in power converters. Noworolski and Sanders [5] proposed replacing the conventional LC tank with an electrostatically coupled micro-fabricated microresonant structure. Piezoelectric transformers, vibrating piezoelectric bars tapped at various positions for voltage transformation [6], can be designed in various types and structures. They are used in place of electromagnetic transformers for applications such as fluorescent lamp inverters [7], [8], ac-adapters [9] and power supplies [10] for power ranges on the order of 10 W.

In this paper, we present a first-order analysis of energy densities of various mechanical and electrical energy storage mechanisms to identify potential passive component technologies for power conversion at MHz frequencies. Kinetic, elastic, electrostatic and magnetic energy storage are considered. To analyze the upper performance limit of each mechanism, we assume best-case scenarios, considering mainly the limits imposed by the properties of high-performance materials currently available for each method, and ignoring the practical limitations such as those regarding current fabrication technology. The goal of this work is to identify opportunities for technology development for future power conversion components and systems and not to provide a design process for power converters. Realizing the potential identified by such analysis may require extensive additional research and development effort.

The analysis of energy density shows that mechanical energy is attractive, but it requires transduction for use in electrical power converters. To consider this, we analyze piezoelectric transduction to couple mechanical and electrical energy. The Butterworth-Van Dyke circuit model for a piezoelectric resonator is described and used in the analysis. To compare the performance of piezoelectric resonators to that of conventional LC resonators, a simple 1:1 resonant switched-capacitor (ReSC) type circuit is used as an example power application to standardize the analysis. This work extends our conference publication [11] by using a more accurate inductor model, considering skin effect in inductor windings and commercially available low-energy-density dielectric, and adding a more extensive study of power output capability in a sample application. The results for the LC resonators with commercial C0G capacitors are then verified using an experimental prototype; the details of the design choices and the small-signal experimental verification are presented in another conference publication [12].

This work was supported by the National Science Foundation under Grant Number 1507773 and 1610719.

The authors are with the Thayer School of Engineering, Dartmouth College, Hanover, NH 03755 USA (e-mail: phyo.a.kyaw.th@dartmouth.edu; aaron.l.stein@dartmouth.edu; charles.r.sullivan@dartmouth.edu)

Color versions of one or more of the figures in this paper are available online at <http://ieeexplore.ieee.org>.

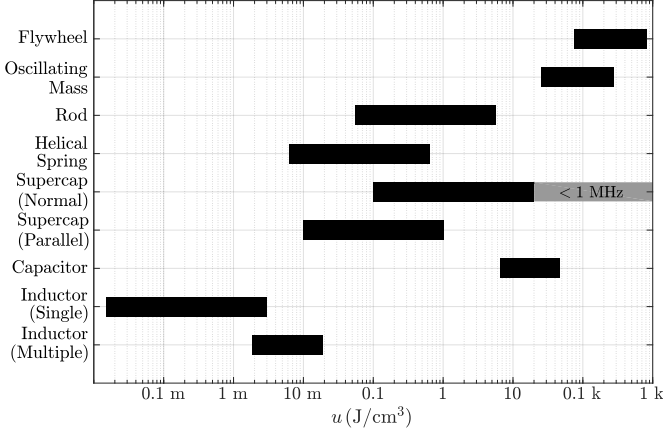


Fig. 1. Comparison of achievable energy densities for different energy storage mechanisms using high performance materials. The energy densities are independent of frequency, with the exception of inductors with a single-layer winding whose energy density depends on the skin depth. The energy densities are limited by material properties or power rating. The normal supercapacitors are limited by the response frequency; the higher the response frequency, the lower the achievable energy density.

II. ANALYSIS OF ENERGY DENSITY

Kinetic, elastic, electrical and magnetic energy storage mechanisms are analyzed in terms of the maximum possible volumetric energy density u . The energy density is based on the volume of the enclosing box of the storage element rather than the volume of the material. For the preliminary analysis in this section, ideal scenarios are considered in order to find upper limits to possible performance that could be achieved with further technological development. These idealizations include mechanical oscillation in vacuum, zero capacitor dielectric loss and zero magnetic core loss, but conduction loss is considered for magnetic energy storage. Later sections explore practical considerations that reduce performance relative to these ideal assumptions. In order to perform a fair comparison, a fixed 1 cm³ volume, 300 V rating and 10 MHz frequency are used to standardize the analysis. This section will summarize the energy density analysis; details are discussed in [11].

A. Mechanical Energy

Kinetic energy stored in mechanisms such as a linearly oscillating mass or a flywheel is proportional to the square of the speed of oscillation or rotation. However, a faster motion requires larger restoring or centripetal forces. This presents an upper limit to the achievable speed, and hence the energy density, depending on the compressive or tensile yield strength of the material σ_y . The energy densities are given by $\sigma_y/2$ for a flywheel and $\sigma_y/6$ for an oscillating mass in vacuum. The factor of three difference is due to the extra space required for oscillation; the difference will be larger if the air drag is considered [11]. For steel, one of the strongest materials, with strength 150 to 1500 MPa [13], the maximum achievable energy density is 75 to 750 J/cm³ for flywheels and 25 to 250 J/cm³ for oscillating masses in vacuum. These energy density ranges are summarized in Fig. 1 together with those of other mechanisms discussed below.

TABLE I
HIGH ENERGY DENSITY CAPACITOR DIELECTRIC MATERIALS

Dielectric Material	ϵ_r	E (V/μm)	u (J/cm³)	Ref
polypropylene	2.2	820	6.5	[14]
alkali-free glass ^a	6	1200	38	[14]
P(VDF-CTFE)/BNNS/BT ^b	12	552	21.2	[15]
PVDF/ArPTU ^c	9.2	700	10.8	[16]

^abarium borosilicate

^bpoly(vinylidene fluoride-co-chlorotrifluoroethylene)/hexagonal boron nitride nanosheets/barium titanate

^cpolyvinylidene fluoride/aromatic polythiourea

For elastic potential energy storage, the energy density depends on the material strength as well as the stiffness. The maximum elastic energy density of a rod is $\sigma_y^2/(2Y)$ where Y is the Young's modulus of the material. For helical springs, torsional yield strength and shear modulus need to be used in place of σ_y and Y respectively. Geometric factors such as the spring index (the ratio of the diameter of the spring coil to that of the wire) and the ratio of the volume of the spring material to that of the box containing the spring also affect the energy density [11]. For steel, with σ_y of 150 to 1500 MPa and Y of around 200 GPa [13], the achievable energy densities are 56 to 5600 mJ/cm³ for rods and 6.3 to 630 mJ/cm³ for helical springs as shown in Fig. 1.

B. Electrostatic Energy

Capacitors' maximum electrical energy density is given by $\epsilon E^2/2$, where ϵ is the permittivity and E the breakdown electric field of the dielectric. Polypropylene, a common low-loss polymer dielectric, has a maximum energy density of around 6.5 J/cm³ with $\epsilon_r = 2.2$ and $E = 820$ V/μm [14]. Recent efforts in enhancing the capacitor energy density involve forming nanocomposites of high-breakdown-field polymers and high-dielectric-constant ceramics [15], [16]. Testing commercially available glass [14] also shows that alkali-free glass has a high energy density. Table I compares the performance of polypropylene and state-of-the-art dielectrics in the literature; these are the energy densities at the breakdown limits and derating is necessary for continuous long-term operation.

Electrolytic double-layer supercapacitors are another way to achieve a high energy density. A permeable separator soaked with an electrolyte is placed between electrodes with a large surface area to volume ratio. The opposite charges are separated by an ion-level thickness between the electrode surface and the electrolyte. Graphene is widely used in supercapacitors due to its large specific surface area of 2675 m²/g [17]. This large surface area means that supercapacitors have very high energy densities, as much as 1 kJ/cm³; however, they usually have large RC time constants on the order of milliseconds to seconds [18], which is too slow for MHz frequency switching. For frequencies higher than 1 MHz, the maximum achievable energy density is about 20 J/cm³.

C. Magnetic Energy

Inductors' maximum energy density depends on the permeability μ and the saturation flux density B_{sat} of magnetic

cores, usually below 1 T. Much higher magnetic flux densities are achievable with air-core inductors but at the expense of high current and conductor losses. Pulsed power systems can have an energy density as much as 39 J/cm³ with a maximum flux density of 50 to 100 T, with the only limitation being “the onset of melting at the conductor surface” [19]. However, such a constraint does not apply in our study of storage mechanisms for use in switching power converters at MHz frequencies since the high temperature will result in failure of the insulation materials. Moreover, the temperature rise of a pulsed power system is limited by thermal mass and the same limit could lead to much higher temperatures in the continuous operation of switching converters. The power loss at a current density high enough to bring about melting of the conductor surface will also be too high to be useful in an efficient switching converter.

Thus, power loss in the continuous operation mode, and the resulting temperature rise, is an important limit to consider. In this paper, we use tolerable power loss per unit area $P_{max} = 3 \text{ W/cm}^2$, estimated based on a survey of commercially available millimeter-scale surface mount resistors in the Digi-Key online catalog [20]. The catalog was scanned to search for resistor series with a clear correlation between power rating and surface area; these correlations range from $P_{rating} \propto A_{surface}^{1/2}$ to $P_{rating} \propto A_{surface}^{3/2}$. For a majority of these series, $P_{rating} \propto A_{surface}$, ranging from 1 W/cm² to 4 W/cm². We choose 3 W/cm² as the tolerable power loss to use in the analysis. This is an aggressive assumption, based on resistors which typically tolerate high operating temperatures. However, as discussed below, inductors have a low energy density even with this assumption of a high tolerable loss.

The power loss in an inductor winding (Fig. 2) is given by

$$P = I^2 \rho_e \frac{2w_L}{l_L t_L}, \quad (1)$$

where I is the current through the winding, ρ_e the resistivity, w_L the inductor width, l_L the inductor length and t_L the conductor thickness that is actively conducting current, which may be limited by skin depth as discussed below. For this analysis, we assume that the design is configured for negligible-proximity-effect loss, and that the core loss is negligible, in order to determine an upper limit on possible performance that might be achievable with improved magnetic materials. Using (1), the maximum magnetic field H_{max} for a tolerable power loss per unit area P_{max} can be obtained:

$$P_{max} = \frac{P}{2 l_L w_L} = \frac{I^2}{l_L^2} \frac{\rho_e}{t_L} \\ H_{max} = \sqrt{\frac{P_{max} t_L}{\rho_e}}. \quad (2)$$

For a hypothetical lossless magnetic material with a saturation flux density B_{sat} , the winding-loss-limited energy density is

$$u = \frac{1}{d_L + 2t_L} \left(d_L + \frac{t_L}{3\mu_{opt}} \right) \frac{1}{2} B_{sat} H_{max}, \quad (3)$$

where the fraction $t_L/(3\mu_{opt})$ is to account for the energy stored in the conductor. This energy density can be achieved

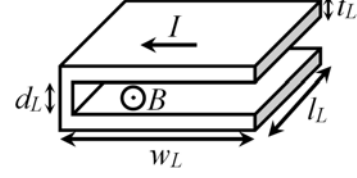


Fig. 2. Sketch of an inductor with a foil winding.

TABLE II
MAGNETIC ENERGY STORAGE DENSITIES

Material	Single-Layer Winding		Multi-Layer Winding	
	μ_{opt}	$u \text{ (mJ/cm}^3\text{)}$	μ_{opt}	$u \text{ (mJ/cm}^3\text{)}$
Air	1	0.015	1	1.87
$B_{sat} = 0.32 \text{ T}$	42	0.97	4	5.8
$B_{sat} = 1 \text{ T}$	11	3	12	17.2

by using an effective permeability $\mu_{opt} = B_{sat}/\mu_0 H_{max}$. Particular values for μ_{opt} can be physically attained by choosing the correct air gap length. For air-core inductors, the saturation flux density B_{sat} is simply $\mu_0 H_{max}$.

At MHz frequencies, the skin depth δ is on the order of tens of micrometers, which limits the effective conductor thickness. However, this skin effect can be partially overcome by using multilayer foil windings [21]. Assuming optimistically that a multilayer technique works perfectly without requiring additional space or incurring any excess power losses, the result could conceivably be equivalent to allowing full use of a conductor much thicker than a skin depth. In this case, the conductor thickness can be optimized for maximum energy density subject to the power loss density constraint. For both single-layer and multi-layer cases, we calculate, and tabulate in Table II, the energy densities for some hypothetical lossless magnetic cores, representing ferrite ($B_{sat} = 0.32 \text{ T}$), and metal and metal-alloy based materials ($B_{sat} = 1 \text{ T}$) [22].

Fig. 1 shows a comparison of achievable energy density ranges for the storage mechanisms discussed above, limited by the properties of high performance materials. Flywheels and oscillating masses provide the highest energy density, about an order of magnitude higher than capacitors, which in turn have an order of magnitude better performance than springs. Inductors provide the lowest energy density of all the mechanisms, about two orders of magnitude lower than springs. It should be noted that the energy density of inductors is calculated using power rating of commercially available resistors in continuous operation whereas other mechanisms are analyzed using electrical or mechanical breakdown. However, even with an order of magnitude derating on other mechanisms for continuous operation, inductors' energy density will still be about an order of magnitude lower than that of springs.

III. RESONANCE, TRANSDUCTION AND EXAMPLE POWER APPLICATION

Typical switching converters for MHz frequencies use an LC resonant tank. An alternative resonant structure with higher energy density and lower losses could enable smaller, more

efficient converters. In an LC or a mass-spring (MK) resonator, the element with the lower energy density typically limits the performance: the inductor in the LC resonator and the spring in the MK resonator. Given that springs have an energy density limit about 300 times higher than that of inductors, MK resonance systems can be better than LC tanks at compactly storing energy with MHz resonance frequencies.

Electromechanical transduction methods need to be investigated to exploit this high-energy-density MK resonance for use in switching power converters. Among electromagnetic, electrostatic and piezoelectric transduction systems, the first can be ruled out since the necessary windings are subject to the same performance limits as inductor windings. Electrostatic systems, though similar to capacitors, have low energy density because of the lack of dielectric. Piezoelectric systems are interesting since they can drive oscillating masses and have a similar energy density limit to that of springs. Although flywheels have the highest energy density of all the mechanisms discussed (Fig. 1), to our knowledge, there is not yet an efficient rotary piezoelectric driving mechanism for the MHz frequency range [23]–[25]. Thus, we study the performance of a piezoelectric resonator to use in an MK resonance system with an oscillating mass. A resonant switched-capacitor type circuit [26], [27] is used as an example power application to compare the performance of the piezoelectric resonator to that of a conventional LC resonator.

A. Piezoelectric Resonator

Fig. 3 (a) shows a piezoelectric resonator in length-extensional vibration mode, in which the direction of vibration and poling are the same, and it can be described by the Butterworth-Van Dyke model shown in Fig. 3 (b). For a resonator vibrating and poled in the thickness d direction, the capacitance C_0 and the motional impedances R , L and C are

$$C_0 = \frac{\epsilon A}{d}, \quad (4)$$

$$R = \frac{\pi^2 d}{8k^2 \epsilon Y A} \eta \rho_m = \frac{\pi^2}{8k^2 C_0} \frac{\eta \rho_m}{Y}, \quad (5)$$

$$L = \frac{d}{8k^2 \epsilon Y A} \rho_m l'^2 = \frac{1}{8k^2 C_0} \frac{\rho_m l'^2}{Y}, \quad (6)$$

$$C = \frac{8k^2 \epsilon Y A}{\pi^2 d} \frac{1}{Y} = \frac{8k^2 C_0}{\pi^2}, \quad (7)$$

where A is the poling area (bl in Fig. 3 (a)), η the kinematic viscosity of the material and the environment, ρ_m the density of the material, Y the Young's Modulus, k^2 the electromechanical coupling coefficient and l' the length of vibration (d for the longitudinal vibration in Fig. 3 (a)) [28].

The resonance frequency f_0 and the quality factor Q derived from (4) – (7) are

$$f_0 = \frac{1}{2\pi\sqrt{LC}} = \frac{1}{2l'} \sqrt{\frac{Y}{\rho_m}}, \quad (8)$$

$$Q = \frac{1}{R} \sqrt{\frac{L}{C}} = \frac{l'}{\pi\eta} \sqrt{\frac{Y}{\rho_m}}. \quad (9)$$

There is a trade-off between the resonance frequency and the quality factor with respect to the length of vibration. A

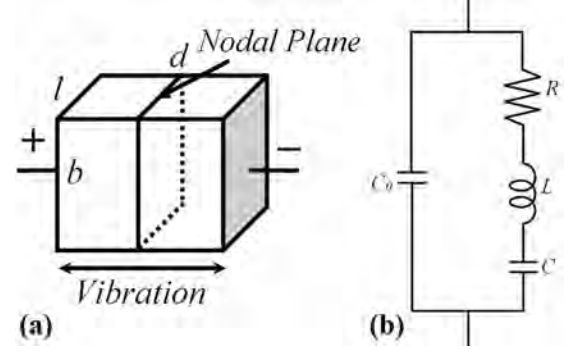


Fig. 3. (a) A piezoelectric resonator with vibration and poling along the same direction (along d). (b) Butterworth-Van Dyke model of a piezoelectric resonator. C_0 is the capacitance between the two electrode plates and R , L and C are motional impedances.

TABLE III
LITHIUM NIOBATE MATERIAL PROPERTY CONSTANTS

ϵ_r^T	Relative permittivity	28
Y	Young's Modulus	2×10^{11} N/m ²
ρ	Density	4700 kg/m ³
ν	Poisson's Ratio	0.241
$f_0 Q$	Figure of Merit (Maximum $f_0 Q$)	1×10^{14}
E	Breakdown electric field	2.6×10^7 V/m
T_y	Yield stress	1.1×10^8 N/m ²
S_y	Yield strain	5.5×10^{-4}

decrease in the length l' increases the resonance frequency and decreases the quality factor. Combining (8) and (9) results in

$$f_0 Q = \frac{Y}{2\pi\eta\rho_m}. \quad (10)$$

This product is a function of the material properties and is independent of the resonator dimensions, so it can be considered as the figure of merit (FoM) for a piezoelectric material. Some research in piezoelectric materials focuses on achieving a high $f_0 Q$ FoM, and values as high as 1.1×10^{14} have been achieved by some groups [29], [30].

Lithium niobate is chosen as the material for analysis due to its high electromechanical coupling coefficient and FoM [29], [31]; its properties are summarized in Table III [29], [30], [32]–[35]. For a 1 cm \times 1 cm \times 1 cm block of lithium niobate, vibrating and poled in the same direction (parallel mode), with an optimistic assumption of $k^2 = 0.3$, the Butterworth-Van Dyke model gives $R = 2.6$ m Ω , $L = 0.40$ H, $C = 0.60$ pF and $C_0 = 2.5$ pF. The resonator has a series resonance at 326 kHz and a parallel resonance at 461 kHz.

For vibration and poling in distinct directions (normal mode), lower impedance can be achieved with the same resonance frequency and volume. For operation in the normal mode, the resonator in Fig. 3 (a) can be poled along the same direction d with vibration along either l or b . The same resonance frequency as that for the parallel mode can be obtained by adjusting the vibration length to account for the difference in the material property constants between the two modes. The impedance can be lowered by reducing the poling

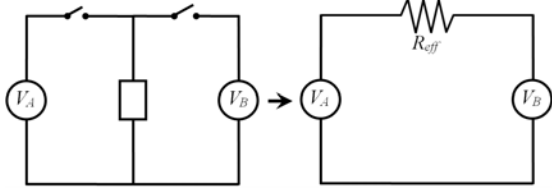


Fig. 4. 1:1 resonant switched-capacitor type circuit used for comparing the mechanical and the electromagnetic resonances.

thickness to the minimum required to sustain the required voltage rating, and connecting multiple layers in parallel. The smaller poling thickness d increases the capacitance C_0 and reduces the motional resistance R while parallel connections allow for further impedance reduction. Some of the practical limitations of this approach are discussed in Section IV-A.

B. Resonant Switched-Capacitor Type Circuit

To determine the potential of the piezoelectric resonator, its performance needs to be compared to that of a conventional LC resonant tank. The performance metrics for comparison are losses in the resonator, and the power output limited by these losses or other mechanical nonlinearities. As a standard for comparison, we use a 1:1 resonant switched-capacitor (ReSC) circuit (Fig. 4) with 300 V nominal input and output voltages [26], [27]. Although we use a 1:1 converter for simplicity, the trends found would apply to a variety of ReSC applications. ReSC converters have recently attracted interest and have shown to be surprisingly versatile [36]–[40]. For example, [39], [40] demonstrate that they can be operated in modes that provide continuous variation of the output voltage.

The process of charge transfer between the input V_A and the output V_B can be characterized by the effective resistance R_{eff} in Fig. 4. This effective resistance is given by

$$R_{eff,C} = \frac{1}{fC} \quad (11)$$

for a capacitor at a frequency f and

$$R_{eff,LC} = \frac{1}{f_0 C} \tanh\left(\frac{\pi}{4Q}\right) = 2\pi\sqrt{\frac{L}{C}} \tanh\left(\frac{\pi R}{4} \sqrt{\frac{C}{L}}\right) \quad (12)$$

for an LC resonator at the resonance frequency f_0 with parasitic resistance R [27]. Because a piezoelectric resonator can be modeled as a capacitor in parallel with a motional LC resonance (Fig. 3 (b)), its effective resistance is

$$R_{eff,piezo} = \left(\frac{1}{R_{eff,C}} + \frac{1}{R_{eff,LC}} \right)^{-1}. \quad (13)$$

The power output of a ReSC-type circuit with dc bias voltage V_{dc} and capacitance C at resonance frequency f_0 is

$$\begin{aligned} P &= \frac{1}{2} C \left((V_{dc} + V_{ac})^2 - (V_{dc} - V_{ac})^2 \right) f_0 \\ &= 2CV_{dc}V_{ac}f_0 = \frac{1}{\pi} V_{dc}I_{ac}, \end{aligned} \quad (14)$$

where V_{ac} is the peak ac voltage across the capacitor and $I_{ac} = V_{ac}\sqrt{C/L}$ the peak ac current through the capacitor.

We have explored various electromechanical transduction methods to exploit the high energy density offered by MK resonance and ruled out the electromagnetic and electrostatic transduction mechanisms respectively due to the winding loss and the low energy density. We also studied the piezoelectric resonator and described an equivalent circuit model. In addition, a ReSC circuit is described as an example power application which can be used to compare the performance of the piezoelectric and the conventional LC resonator.

The two resonators are compared in the following sections. In the analysis, an air-core inductor and a capacitor with alkali-free glass dielectric [14] are used for the LC resonator and lithium niobate [32] is used for the piezoelectric resonator. A dc voltage rating of 300 V is assumed for both resonators.

IV. RESONANT SWITCHED-CAPACITOR TYPE CIRCUIT: EFFECTIVE RESISTANCE

A. Effective Resistance of a Piezoelectric Resonator

The effective resistance of a piezoelectric resonator (Fig. 3 (a)) in a ReSC-type circuit at a resonance frequency f_0 can be derived from (11)–(13):

$$R_{eff,piezo} = \left(f_0 C_0 + f_0 C \coth\left(\frac{\pi}{4Q}\right) \right)^{-1}. \quad (15)$$

Assuming a high quality factor ($Q \gg 1$) and using (4) and (7), the expression can be simplified:

$$\begin{aligned} R_{eff,piezo} &\approx \frac{1}{f_0 C_0} \left(1 + \frac{8k^2}{\pi^2} \frac{4Q}{\pi} \right)^{-1} \\ &\approx \frac{\pi^2}{8k^2 C_0} \frac{1}{2\pi f_0 Q} \frac{\pi^2}{2} = \frac{\pi^2 R}{2}, \end{aligned} \quad (16)$$

where R is the motional resistance described in (5). Thus, the effective resistance of a high Q piezoelectric resonator in a ReSC-type circuit depends only on the capacitance C_0 , the electromechanical coupling coefficient k^2 and the $f_0 Q$ FoM.

For a particular material (i.e. fixed k^2 and $f_0 Q$), the lowest R_{eff} can be obtained by maximizing C_0 . This is achievable by connecting multiple piezoelectric layers in parallel, each of which has a poling thickness of $d = V/E$ to sustain a voltage rating V . For lithium niobate (Table III), we get $d = 11.5 \mu\text{m}$ and $R_{eff} = 18 \mu\Omega$ for a 1 mm^3 volume assuming optimistically that $k^2 = 0.3$. This R_{eff} , normalized by volume, is constant for a particular material. Since vibration and poling do not have to be in the same direction (for example, vibration along l and poling along d in Fig. 3 (a)), the length of vibration l' can be varied independent of the poling thickness d . Thus, the low effective resistance of $18 \mu\Omega$ can theoretically be achieved with 1 mm^3 volume of lithium niobate independent of the resonance frequency.

However, the above analysis only considers the $f_0 Q$ FoM and the electrical breakdown of a piezoelectric resonator, and is an optimistic lower bound on the achievable R_{eff} . The Butterworth-Van Dyke model in (4)–(7) is specific to length-extensional vibration and some material property constants in Table III are for a specific orientation of the piezoelectric resonator. The normal mode, with poling and vibration in different directions, may correspond to less favorable material

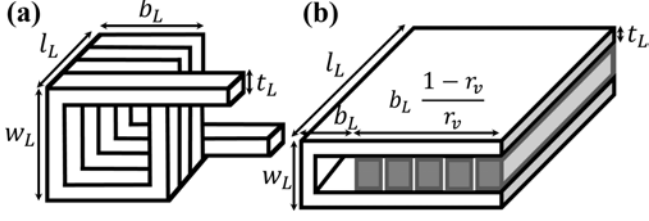


Fig. 5. Resonator sketches. (a) A multiple-turn inductor for high inductance. (b) A single-turn inductor for low inductance in parallel with arrays of reference capacitors (the capacitor self-inductance is not negligible).

property constants and result in a higher effective resistance. Moreover, because the analysis assumes a multilayer piezoelectric resonator, the poling electrodes contribute to the motional resistance. The specific mounting position of the resonator on the base substrate may also affect the kinematic viscosity η and the FoM. These technological constraints need to be overcome first to realize the low effective resistance of the lithium niobate piezoelectric resonator mentioned above.

B. Effective Resistance of an LC Resonator

An electromagnetic resonator as shown in Fig. 5 comprises a capacitor and an air-core inductor in a total volume \mathcal{V} . The volume of the inductor is a particular fraction r_v of the total volume while that of the capacitor equals $(1 - r_v)\mathcal{V}$. For a particular volume \mathcal{V} , voltage rating V and resonance frequency f_0 , the capacitor dielectric type determines the achievable energy density and the inductor can be designed to obtain the desired resonance frequency. We assume a 300 V rating to standardize the analysis.

1) *Capacitor Model*: The achievable energy density of a dielectric material can be represented by capacitance C_{ref} , voltage rating V_{ref} and volume \mathcal{V}_{ref} of a reference capacitor of that particular dielectric type. For the alkali-free glass dielectric discussed in Section II-B, C_{ref} , V_{ref} and \mathcal{V}_{ref} can be obtained from the dielectric constant and the breakdown field. For commercially available C0G and X7R capacitors, Digi-Key online catalog for surface mount capacitors [41] can be scanned to obtain a capacitor with the highest energy density. Limiting the voltage rating to lower than 400 V to address a wide range of application, the C0G and X7R capacitors with highest energy density are C2012C0G2E103K125AA from TDK and 12061C225KAT2A from AVX respectively (Table IV). It is assumed that these capacitors can be redesigned to obtain the 300 V rating for the analysis. These reference capacitors, connected in parallel in a volume $(1 - r_v)\mathcal{V}$, give the capacitance

$$C = C_{ref} \frac{V_{ref}^2}{V^2} \frac{(1 - r_v)\mathcal{V}}{\mathcal{V}_{ref}}. \quad (17)$$

For X7R capacitors, the degradation of the dielectric at high frequency and operating voltage can be reflected by multiplying C_{ref} with a relevant factor. This can be obtained from experimental measurements or from manufacturer design tools, namely TDK SEAT2013 [42] and AVX Spicap 3.0 [43].

The effective series resistance of the capacitor R_C can be due to conductor plate resistance and dielectric dissipation

TABLE IV
REFERENCE CAPACITORS

Dielectric	C_{ref} (nF)	V_{ref} (V)	\mathcal{V}_{ref} (mm ³)	u (J/cm ³)
Glass	849.6	300	1	38
C0G	10	250	3.625	86.2 m
X7R	2200	100	4.813	2.29

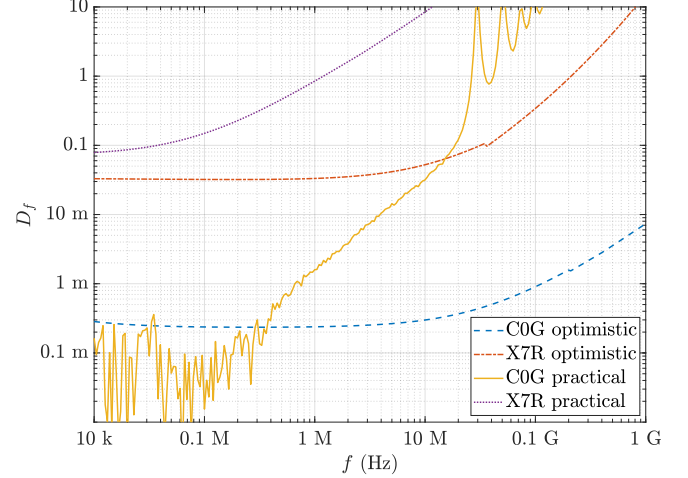


Fig. 6. Dissipation factor of C0G and X7R dielectric in optimistic scenarios respectively based on Kemet C0402C279K8GAC and C0805C103KCRAC capacitors [44], and for practical implementations based on the reference capacitors in Table V, to be discussed in Section VI.

factor. The former can usually be ignored because of the parallel connections among conductor plates. The latter can be calculated from the dielectric dissipation factor D_f , giving

$$R_C = \frac{D_f}{2\pi f_0 C}. \quad (18)$$

The dissipation factor of C0G and X7R dielectric materials can be extracted from the ESR data of some reference capacitors; these reference capacitors are distinct from the capacitors in Table IV. To obtain approximately the intrinsic loss in the dielectric rather than the conductor plates, these reference capacitors should have a small capacitance and a large voltage rating in a small case size. We use Kemet K-Sim design tool [44] to extract the ESR and D_f data (Fig. 6). Table IV and Fig. 6 together give an optimistic combination of high energy density and low dissipation factor; this combination does not correspond to any commercially available capacitors.

2) *Inductor Model*: The inductor needs to be designed such that it gives the resonance frequency f_0 when combined with the capacitance in (17). This requires

$$L = \frac{1}{4\pi^2 f_0^2 C} = \frac{N^2 K \mu (w_L - 4t_L/3)(b_L - 4t_L/3)}{l_L}, \quad (19)$$

where N is the number of turns in the inductor winding and K Nagaoka's coefficient, which is the correction factor for end effects in an air-core coil of finite length [45]. K equals 1 for narrow and long coils ($l_L \gg w_L$, b_L) and decreases as the coil gets shorter and wider.

Low resonance frequencies require a large inductance, which, given a constrained volume $r_v\mathcal{V}$, can be achieved by

using a multiple-turn winding ($N > 1$) as shown in Fig. 5 (a). In this case, the capacitor self-inductance is negligible and the two sides b_L and w_L of the inductor are qualitatively the same so we can set $w_L = b_L$. From the required volume $r_v \mathcal{V}$, we can obtain $l_L = r_v \mathcal{V} / w_L^2$. Thus, (19) can be rewritten as

$$L = \frac{N^2 K \mu w_L^2}{r_v \mathcal{V}} \left(w_L - \frac{4t_L}{3} \right)^2. \quad (20)$$

The inductor ESR equals the conductor resistance

$$R_L = \frac{N^2 \rho_e 4(w_L - t_L) w_L^2}{t_L r_v \mathcal{V}}, \quad (21)$$

where ρ_e is the resistivity of the conductor.

For higher frequencies, only a small inductance is required, which usually limits the number of turns to one. In this case, the capacitor self-inductance needs to be considered; a parallel resonator in this scenario is shown in Fig. 5 (b), which has

$$\begin{aligned} L &= \frac{K \mu_0 w_L b_L}{r_v \mathcal{V}} \left(w_L - \frac{4t_L}{3} \right) \left(b_L + b_L \frac{1 - r_v}{3r_v} - \frac{2t_L}{3} \right), \\ &= \frac{K \mu_0 w_L b_L}{r_v \mathcal{V}} \left(w_L - \frac{4t_L}{3} \right) \left(b_L \frac{1 + 2r_v}{3r_v} - \frac{2t_L}{3} \right). \end{aligned} \quad (22)$$

The $b_L(1 - r_v)/(3r_v)$ term is a first-order approximation for the effective breadth of the capacitors that contribute to the total inductance. The factor of 3 results from the assumption that the current is equally distributed among the capacitor electrode plates, resulting in a magnetic field that increases linearly and a magnetic energy density that increases quadratically along b_L , which, when integrated, gives a factor of 3 in the denominator. The inductor ESR in this case is

$$R_L = \frac{\rho_e w_L b_L}{r_v t_L} \left(w_L + 2b_L \frac{1 + 2r_v}{3r_v} \right). \quad (23)$$

3) Resonator Optimization: The effective resistance of the LC resonator in a ReSC circuit can be calculated by substituting (17)–(23) into (12). $R_{eff,LC}$ depends on the following: the resonator volume \mathcal{V} , the dielectric type, the inductor-resonator volume ratio r_v and the inductor geometry (N , w_L , b_L and t_L). According to (19), N can be expressed in terms of w_L , b_L and t_L . Thus, for a fixed volume \mathcal{V} and dielectric type, the design of the LC resonator depends on four independent variables (r_v , w_L , b_L , t_L), which can be used to optimize the resonator performance.

We perform particle swarm optimization [46] with respect to these parameters to determine the minimum R_{eff} of an LC resonator as a function of the resonance frequency for a 300 V rating and fixed volumes. Fig. 7 shows the optimization results for the ideal scenario: an inductor that is not skin-effect limited (i.e. using a multilayer foil winding [21] discussed in Section II-C) and a lossless capacitor with the high-energy-density alkali-free glass dielectric (Table I and IV). Each fixed-volume curve has two distinct sections: a larger slope at the lower frequency end and a smaller slope at the higher frequency end. The inductor designs for the boundary between these two sections are a single-turn inductor with an approximately cubic shape (Fig. 7 (c)). As the frequency decreases, the number of turns remain constant at one, and the coil becomes shorter and wider ($w_L = b_L > l_L$). As the

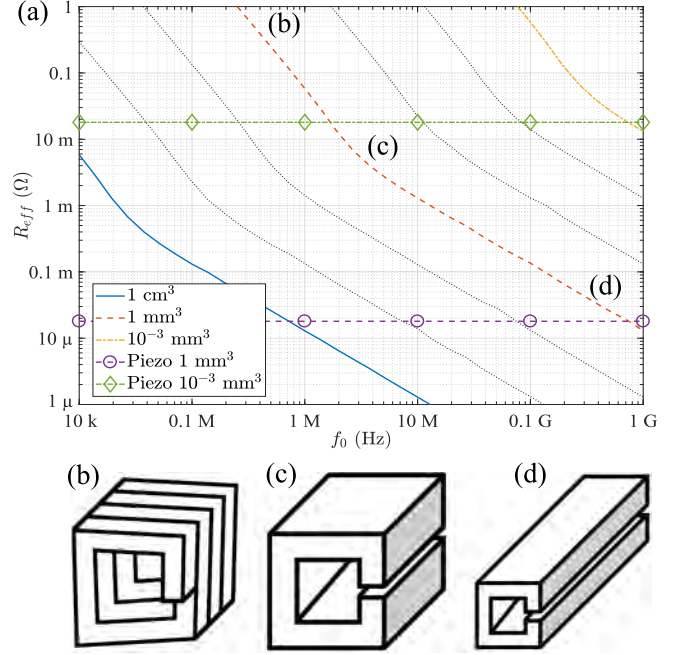


Fig. 7. (a) Optimal effective resistance vs. resonance frequency of an LC resonator and a piezoelectric resonator with 300 V rating and volumes from 1 cm^3 to 10^{-3} mm^3 . The optimization assumes an air-core inductor with no skin-effect limit and a lossless capacitor with alkali-free glass dielectric. (b)–(d) Representative inductor designs for each section of the plot.

coil becomes very short, further decreases in the frequency are achieved by increasing the number of turns in the windings while keeping the dimensions fixed ($w_L = b_L \gg l_L$, Fig. 7 (b)). At frequencies higher than the boundary, the inductors have a single-turn winding, and becomes thinner and longer ($w_L = b_L \ll l_L$, Fig. 7 (d)) as the frequency increases. The curve roughness in the higher frequency portion is due to the accuracy limit in the optimization routine and does not relate to a physical phenomenon.

This relation between the minimum effective resistance and the resonance frequency for a fixed volume can be explained as follows. Because the capacitor ESR R_C is assumed to be zero, design changes along each fixed-volume curve is mostly due to changes in the inductor geometry. A large inductance required for low resonance frequencies is obtained using an inductor with a multiple-turn winding with a cross-section larger than the length ($w_L = b_L > l_L$), resulting in a large R_{eff} at the low-frequency end. As the frequency increases, the inductance is decreased by reducing the number of turns, thereby reducing R_{eff} . As the number of turns approaches one, the self-inductance of capacitors becomes significant, reducing the required lumped inductance and the corresponding inductor ESR, thereby pushing the R_{eff} vs. f_0 curve downwards around the knee in the curve. As the frequency gets higher, the number of turns remains at one and further decreases in L and R_{eff} are achieved by decreasing the inductor cross-sectional area (w_L , b_L) and increasing its length l_L , resulting in a change in the slope of the curve. Another contribution to the difference between the two sections is the Nagaoka's coefficient K , which approaches 1 as the inductor becomes narrower and longer with increasing frequency.

According to Fig. 7, very low effective resistances can theoretically be achieved at high frequencies; however, there are practical limitations regarding the inductor designs. For example, R_{eff} as low as $1.32 \mu\Omega$ can be achieved at 100 MHz in a 0.1 cm^3 volume, but only with impractical dimensions of $0.22 \text{ mm} \times 0.22 \text{ mm} \times 0.86 \text{ m}$. Because the optimal inductor is very thin and long, it can also be constructed by a parallel connection of multiple shorter inductors without significantly affecting the performance; for instance, 200 $0.22 \text{ mm} \times 0.22 \text{ mm} \times 4.3 \text{ mm}$ in parallel will give the same R_{eff} with a more practical aspect ratio. However, implementing the parallel connections usually requires additional space and results in higher effective resistances. Thus, Fig. 7 shows optimistic physical limits of LC resonator performance in the ideal scenario of an inductor with no skin-effect limit and a lossless high-energy-density alkali-free glass dielectric without the practical constraints regarding aspect ratios or implementation of parallel connections.

In order to obtain the performance limit of the LC resonant tank rather than that of the ReSC converter, switching losses are not considered in this analysis. As a result, the effective resistance gets significantly lower at higher frequencies, but only with impractical aspect ratios as described above. And at MHz switching frequencies, the switching losses may be higher than the effective resistance presented in Fig. 7 even if zero-voltage switching (ZVS) is used to minimize losses [47]. Thus, very high switching frequencies may not be favorable for designing practical ReSC converters considering all the losses, and Fig. 7 is to be regarded as the performance limits of the resonators themselves, independent of any assumptions about semiconductor technology.

This optimization process is repeated with various modifications to determine the effect of various assumptions in the ideal scenario and the results for 1 cm^3 volume are plotted in Fig. 8. We first remove the ideal inductor assumption, i.e. a perfect multilayer foil winding that allows full use of a conductor much thicker than skin depth. Adding the skin-effect limit increases R_{eff} by a factor of five at the high-frequency end.

Keeping the skin-effect limit, we examine the effect of changing various assumptions regarding the capacitor. First, the capacitor dielectric is changed from glass to commercial C0G and X7R dielectric materials. The difference in the energy densities among the three dielectric types translates to a difference in achievable R_{eff} . This is because for the same resonance frequency, a lower-energy-density dielectric needs a larger inductance than a higher-energy-density dielectric does, and larger inductance usually results in higher ESR as discussed above. Second, the degradation of X7R capacitors with respect to operating voltage and frequency effectively reduces the capacitor energy density, resulting in a factor of 3.5 increase in R_{eff} . Third, adding the capacitor loss (18) does not change R_{eff} at the low-frequency end but increases R_{eff} at the high-frequency end due to the frequency dependence of the capacitor dissipation factor (Fig. 6). The effect of capacitor loss is also more pronounced for X7R capacitors than for C0G capacitors since the dissipation factor is larger.

It is important to emphasize that the dissipation factors and the energy densities used in the analysis for Fig. 8

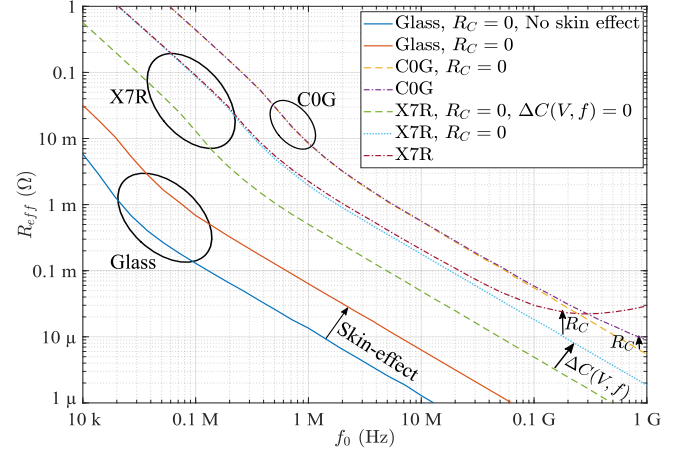


Fig. 8. Optimal effective resistance vs. resonance frequency of an LC resonator with 300 V rating and 1 cm^3 volume. The effects of skin-effect limit, C0G and X7R dielectric energy density, and capacitor losses are examined.

correspond to distinct reference capacitors. Thus, the “C0G” and “X7R” curves in Fig. 8 is an optimistic lower bound on achievable R_{eff} for these capacitor types, calculated using the highest energy density combined with one of the lower dissipation factors found in commercial catalogs. For practical implementation, the energy density and the dissipation factor need to correspond to the same reference capacitor, which will invariably increase the achievable R_{eff} . The results for a practical implementation will be discussed in Section VI.

C. Effective Resistance Comparison

We have modeled and calculated the best possible performance of piezoelectric and LC resonators, with optimistic assumptions, in fixed volumes. Fig. 7 (a) shows the effective resistance vs. frequency plots of both piezoelectric and LC resonators of volumes ranging from 1 cm^3 to 10^{-3} mm^3 for comparing the performance of the two resonator types.

The effective resistance for the piezoelectric resonators, calculated using the Butterworth-Van Dyke model in Section III-A is independent of frequency and is inversely proportional to the total volume. According to Fig. 7, the piezoelectric resonator outperforms the conventional LC resonator in terms of R_{eff} below 750 MHz. It should be noted that Fig. 7 shows the optimistic lower bounds on the R_{eff} at various resonance frequencies for LC and piezoelectric resonators. Adding various practical constraints will increase the achievable R_{eff} , as shown in Fig. 8 for LC resonators.

We have analyzed a ReSC-type circuit with a piezoelectric resonator or an LC resonator in terms of R_{eff} . In the optimistic scenarios without considering practical implementation constraints, both resonators have the potential for a low effective resistance, orders of magnitude better than today’s passive components. The optimistic assumptions include a perfect multilayer piezoelectric resonator without motional resistances of the poling electrodes, a capacitor with a high energy density dielectric, and a perfect multilayer winding with thin foils and equal current sharing. Thus, these results should be interpreted

as the performance limit of piezoelectric and LC resonators without considering the current technological constraints.

V. RESONANT SWITCHED-CAPACITOR TYPE CIRCUIT: POWER THROUGHPUT

Because the effective resistances of the resonators are very small, the more suitable comparison may be in terms of power throughput. The limitations on power include nonlinearity and mechanical fracture for the piezoelectric resonator, dielectric breakdown for the LC resonator, and efficiency and thermal effect of loss for both. Dielectric breakdown is already considered in terms of voltage rating of reference capacitors V_{ref} so will not be described explicitly in this section. The piezoelectric equations in (4)–(10) are only valid for small linear vibrations and high power may push the resonator into the nonlinear regime; extreme vibrations may even cause mechanical breakdown. Efficiency specifications and tolerable thermal effect of loss also limit the current that can be handled. The minimum of these limits sets a constraint on the power handling capability of piezoelectric and LC resonators.

A. Piezoelectric Resonator: Nonlinearity and Yield Strain

To account for nonlinearity in a piezoelectric resonator, the spring constant can be expanded into higher order terms. For a vibration amplitude x , the elastic force acting on an object can be expressed as $k_0x(1 + k_1x + \dots)$ where k_0 is the linear term and k_1 the first-order anharmonic term of the spring constant. As a condition for unacceptable nonlinearity, we use the bifurcation point above which a small change in the initial conditions may cause a jump in the amplitude of the steady state vibration [48]. The critical vibration amplitude before the vibration becomes nonlinear is given by

$$x_c = \sqrt{\frac{16}{5\sqrt{3}k_1^2Q}}, \quad (24)$$

where Q is the quality factor of the resonance [48]. For a bulk acoustic wave (BAW) resonator as shown in Fig. 3 (a),

$$k_0 = \frac{\pi^2 A' Y}{2l'} \quad \text{and} \quad k_1 = -\frac{8\pi\nu}{3l'}, \quad (25)$$

where A' is the cross-sectional area of vibration (bl in Fig. 3 (a)), l' the vibration length and ν Poisson's ratio [48]. Combining (24) and (25), we can solve for the maximum strain based on this nonlinearity limit for the piezoelectric resonator,

$$S_c = \frac{x_c}{l'} = \sqrt{\frac{16}{5\sqrt{3}Q}} \frac{3}{8\pi\nu} = \sqrt{\frac{16}{5\sqrt{3}f_0Q}} \frac{3}{8\pi\nu} \sqrt{f_0}. \quad (26)$$

Below this strain level, operation can be considered approximately linear. Above it, nonlinearity makes operation difficult. Operation in the nonlinear range might be feasible, but we find that there is little motivation to develop this capability, once other limitations and design considerations are included.

The other limit on maximum allowable strain is the yield strain S_y . It can be seen from (26) that for a material with a particular value of the f_0Q FoM, the nonlinear strain limit varies with $\sqrt{f_0}$. Thus, S_y rather than S_c becomes the limiting

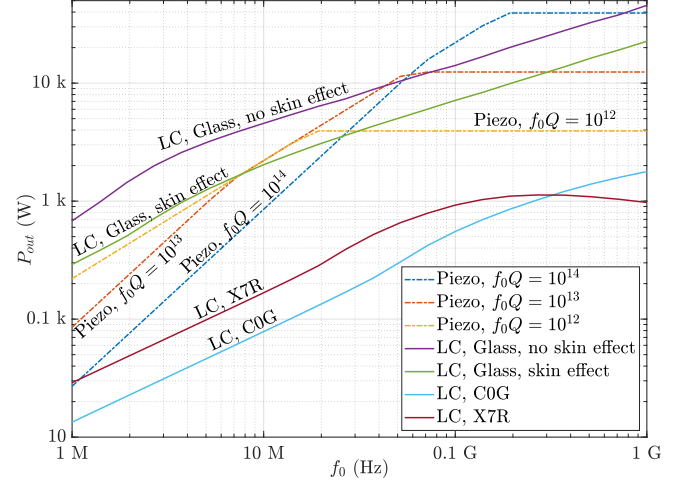


Fig. 9. Maximum power output vs. resonance frequency for piezoelectric and LC resonators with 300 V rating and 1 mm³ volume. Lithium niobate is assumed for the piezoelectric resonator. The three sections of the piezo curves with different slopes corresponds to power output limits due to nonlinearity, the yield strain and the thermal effect of loss. The LC resonator power output is limited by the thermal effect of loss.

constraint at higher frequencies. We define the lower of these two strain limits as the maximum allowable strain S_{max} .

Since C and L in the Butterworth-Van Dyke model of a piezoelectric resonator (Fig. 3 (b)) corresponds to the stored mechanical energy, the maximum vibration amplitude x_{max} , and hence S_{max} , can be translated into the maximum ac voltage V_{ac} or ac current I_{ac} that can be sustained in the resonator. By equating the vibrational energy stored in the piezoelectric resonator at the maximum amplitude $k_0x_{max}^2/2$ to the energy stored in the motional inductance at the ac current limit $LI_{ac}^2/2$, we get

$$I_{ac} = V_{ac} \sqrt{\frac{C}{L}} = \sqrt{\frac{4k^2\pi^2\epsilon Y^2}{\rho_m d(d+2t)}} \frac{\nu S_{max}}{l'}, \quad (27)$$

where d is the poling thickness, t the electrode thickness and l' the vibration amplitude. The power output of the piezoelectric resonator can be calculated by substituting (27) into (14).

Fig. 9 shows the power throughput of a 1 mm³ lithium niobate piezoelectric resonator with a 300 V rating and different values of the f_0Q FoM (10^{12} , 10^{13} and 10^{14}). The curve for each value of f_0Q can be divided into three sections. At the low-frequency end, the resonator is limited by nonlinearity. Because the ac current limit I_{ac} is proportional to $S_{max} = S_c \propto \sqrt{f_0}$ (26) and is inversely proportional to $l' \propto 1/f_0$ (8), $P \propto f_0^{3/2}$ in this nonlinearity-limited section. As the frequency gets higher, the nonlinear strain limit S_c gets larger and the yield strain becomes the binding limit. Because the yield strain is independent of the frequency, the ac current limit only varies with $1/l'$, and hence $P \propto f_0$. Thus, the slope of the middle section is smaller than that of the first section in Fig. 9. At the high-frequency end, the power output is independent of frequency and is limited by the thermal effect of loss, which will be discussed in Section V-B.

To calculate the power output for each value of the f_0Q

FoM (Fig. 9), we have used the minimum of the nonlinearity, the yield strain and the thermal limits at each frequency. However, if a higher R_{eff} is tolerable, the nonlinearity limit can be ignored. Because $f_0Q = 10^{14}$ (Table III) is the highest achieved with lithium niobate and lower f_0Q products are often obtained, it is possible to design a piezoelectric resonator with any lower f_0Q value. As shown in (16), (26) and (27), a lower f_0Q increases the nonlinearity limited power output, but only at the expense of a higher R_{eff} . For instance, the yield strain limited power output at 10 MHz is 2.2 kW whereas the nonlinearity limited power output for $f_0Q = 10^{14}$ is 0.85 kW (Fig. 9). Thus, the nonlinear power limit of the piezoelectric resonator at 10 MHz may be increased by as much as 2.6 times if we use $f_0Q = 10^{14}/2.6^2 \approx 1.5 \times 10^{13}$. Thus, by varying the f_0Q product for each frequency, the piezoelectric resonator can be designed such that the power output is limited only by the yield strain and the thermal effect of loss.

B. Thermal Effect of Loss

Power dissipation in the effective resistance of the piezoelectric and the LC resonators increases the temperature of the resonators. This thermal effect limits the power loss that can be sustained, which in turns limits the power output. The tolerable power loss per unit surface area (Section II-C), and the resonators' effective resistance and dimensions can be used to calculate the maximum ac current through the resonator, and hence the thermal effect limited power output.

As discussed in Section IV-B, long-solenoid inductors can be redesigned using a parallel connection of multiple shorter inductors without impacting the achievable R_{eff} . Thus, for designs with long-solenoid inductors, it is assumed that the inductors are redesigned into an approximately cubic shape. We use this minimum area to calculate the tolerable winding loss of the inductors in the long-solenoid regime.

The thermal effect limited power output of the resonators are included in Fig. 9 together with other limits discussed above. Each "Piezo" curve, which assumes 10 mm² surface area for 1 mm³ volume, is limited by the thermal effect of loss at the high-frequency end. This thermal limit is independent of frequency since the optimal R_{eff} of a piezoelectric resonator does not depend on the frequency (16). The LC resonators, however, have frequency dependent thermal limits since R_{eff} of the LC resonators varies with the frequency.

C. Discussion

Fig. 9 can be used to compare LC and piezoelectric resonators in terms of power throughput. In the most optimistic scenarios for both resonators, the piezoelectric resonator outperforms the LC resonator both in terms of power throughput and effective resistance in the frequency range 45–750 MHz. Although piezoelectric resonators have lower R_{eff} than LC resonators, they are limited by nonlinearity and yield strain at lower frequencies, resulting in a lower power output than the LC resonators. Nevertheless, both resonators have the potential for power densities that are orders of magnitude higher than passive components in use today, subject to the caveats noted below.

The high power density of the piezoelectric resonator can be explained by the low R_{eff} enabled by the perfect multilayer resonator we have assumed. Practical considerations such as the mounting position on the substrate and the poling electrodes may introduce additional motional resistances, which in turn will decrease the thermal limit for the power output.

For the LC resonator, one explanation for the favorable power output is the high energy density of the capacitor. The above analyses assume a capacitor with alkali-free glass dielectric which has a breakdown electric field of 1.2 V/nm, which allows for a very high energy density of 38 J/cm³ (Table I). This is many times higher than the energy density of commercially available capacitors: around 2.3 J/cm³ for X7R ceramic capacitors and 0.086 J/cm³ for C0G capacitors (Table IV). Using these commercially available capacitors decreases the achievable capacitance, which in turns increases the required inductance for a particular frequency, resulting in a higher effective resistance and a lower thermal effect limited power output as shown in Fig. 8 and Fig. 9.

The example power circuit we have chosen for the analysis, namely the resonant switched-capacitor type circuit, also contributes to the very high power output limit. Because of the dc bias, a ReSC-type circuit can be operated with an LC resonance in which the power processed by the capacitor and the inductor may be different by orders of magnitude. For example, for a 1 mm³ LC resonator with an air-core inductor and skin-effect limit at 10 MHz, the optimal design has a capacitance of 777 nF, an inductance of 326 pH and a series resistance of 1.3 mΩ, and can sustain an ac peak current of 21.3 A. In this design, the inductor only stores a maximum energy of 74.1 nJ and processes 0.74 VA at 10 MHz whereas the capacitor processes as much as 2.04 kVA (14). The fact that such a large difference is possible with a ReSC-type circuit is favorable since capacitors have orders of magnitude higher energy density than do inductors.

In non-ReSC-type circuits, such as series resonant converters, a small inductance and a large capacitance mean that the loaded quality factor of the circuit will be too small for useful power conversion. For instance, the LC resonator discussed above only has a characteristic impedance of 20.5 mΩ and an unloaded quality factor of 15.5. To achieve a high loaded quality factor for a large load using a series resonant converter, the inductance-to-capacitance ratio needs to be much larger. Because the underlying loss model is also valid for the series resonant converter, the optimization in Figs. 7, 8 and 9 can be repeated with a minimum loaded quality factor constraint for a series resonant converter. This additional constraint may reduce the achievable power output of the resonator. Thus, the ReSC-type circuit plays a significant role in achieving the high power output discussed in this section.

VI. EXPERIMENTAL RESULTS

A. Design Choices

We built a prototype LC resonator to verify the low effective resistance predicted by Fig. 7 and Fig. 8. However, the results in Section IV-B are based on optimistic assumptions; even the results for resonators using C0G and X7R capacitors are optimistic because of the combination of highest energy density

TABLE V
REFERENCE CAPACITORS FOR EXPERIMENTAL VERIFICATION

Type	Manufacturer	Part Number	C_{ref} (μF)	V_{ref} (V)	Size (mm \times mm \times mm)	u (J/cm ³)
C0G	TDK	CGA9N4C0G2E154J230KN	0.15	250	$5.7 \times 5 \times 2.5$	65.8 m
X7R	AVX	22201C106MAT2A	10	100	$5.7 \times 5 \times 2.79$	628.8 m

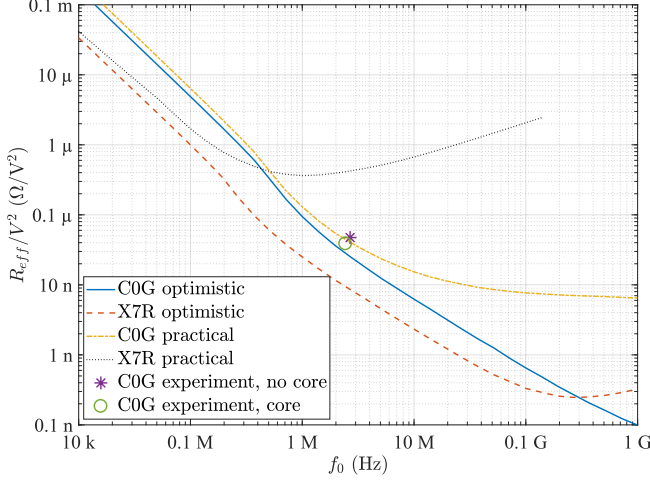


Fig. 10. Minimum achievable R_{eff} normalized by V^2 vs. resonance frequency for LC resonators with 1 cm³ volume. The plots include results for optimistic lower bounds on R_{eff} of LC resonators using C0G and X7R capacitors, theoretical values of R_{eff} using capacitors in Table V and experimentally measured R_{eff} for resonators using the C0G capacitor in Table V.

and low dissipation factor found in online catalogs. Moreover, the volumes of the reference capacitors used in the analysis (Table IV) are also very small for practical implementation of a prototype. Thus, for experimental verification, we choose different reference capacitors with larger volumes (at least 50 mm³) that have maximum energy density with voltage ratings lower than around 3–400 V (Table V). The dissipation factors for these reference capacitors are extracted from TDK SEAT2013 [42] and AVX Spicap 3.0 [43] software and are shown in Fig. 6. More detailed explanations of the capacitor choice and the small-signal experimental verification can be found in [12].

The energy density and the dissipation factors for these new reference capacitors are used to calculate the effective resistance of an LC resonator with skin-effect limited conductor that can be practically implemented, and the results are shown in Fig. 10. For comparison, the figure also includes R_{eff} for optimistic resonators with C0G and X7R capacitors from Section IV-B. Because the voltage ratings for the resonators are different, R_{eff} is normalized by V^2 in Fig. 10, which gives a function proportional to loss fraction. For LC resonators using C0G and X7R capacitors, the practically achievable R_{eff} and optimistic lower bounds are similar for low frequencies ($\lesssim 100$ kHz). However, at higher frequencies, the achievable R_{eff} are orders of magnitude different, mainly because the dissipation factors for off-the-shelf capacitors with high energy density are higher than the optimistic dissipation factors, as shown in Fig. 6.

We verified the results for the resonator with C0G capacitors because they have lower ESR than do X7R capacitors at MHz

TABLE VI
EXPECTED AND MEASURED RESULTS

	Expected	Measured (no core)	Measured (core)
L (nH)	1.2	1.48	1.89
C (μF)	2.4	2.35	2.35
f_0 (MHz)	2.97	2.70	2.40
R_L (m Ω)	0.28	–	–
R_C (m Ω)	0.16	–	–
$R_{esr} = R_L + R_C$ (m Ω)	0.44	0.56	0.45
$R_{eff} = \pi^2 R_{esr}/2$ (m Ω)	2.17	2.76	2.22
$R_{epr} = L/(CR_{esr})$ (Ω)	1.07	1.13	1.76



Fig. 11. The prototype parallel LC resonator using capacitors in Table V.

frequencies. We chose a design with a predicted resonance frequency of around 3.35 MHz with $R_{eff} \approx 2.2$ m Ω , because the effective resistance is in the low single-digit m Ω and the lower R_{eff} at higher frequencies will be much harder to measure. The particular resonator design allocates most of the volume to the capacitors, which means that the capacitor self-inductance is enough for resonance at around 3 MHz. The design requires connecting 14 C0G capacitors (Table V) in a 4×3.5 grid, which is impossible using the selected reference capacitors. Thus, we chose to connect 16 capacitors in a 4×4 grid as shown in Fig. 11. This increases the total volume to 1.14 cm³, which slightly shifts the “C0G practical” curve in Fig. 10 downwards; however, this shift is negligible in the order-of-magnitude plot in Fig. 10. Table VI shows the expected resonance frequency and various impedances of the resonator. The table also includes the impedance at resonance of a parallel resonator with the same inductance, capacitance and loss mechanisms, represented by R_{epr} .

We built a parallel resonator (Fig. 11) considering ease of measuring the 1.07 Ω R_{epr} compared to the 0.44 m Ω R_{esr} . A series resonator with the same inductance and capacitance can be obtained by removing the copper foil at the top of the resonator. The measured impedance at resonance of the parallel resonator can then be used to calculate the ESR of the series resonator, which in turn can be used to calculate R_{eff} of the ReSC converter.

B. Small Signal Test

The resulting parallel resonator was characterized using an Agilent 4294A impedance analyzer. The resonator has a parallel resonance at 2.70 MHz with a parallel impedance $R_{epr} = 1.13 \Omega$ and a measured capacitance $C = 2.35 \mu\text{F}$, resulting in $L = 1.48 \text{ nH}$. These measured impedance values translate to $R_{esr} = 0.56 \text{ m}\Omega$ for the corresponding series resonator and $R_{eff} = 2.76 \text{ m}\Omega$ at 2.70 MHz for a ReSC converter using this series resonator, as shown by the asterisk in Fig. 10. These measured results are also included in Table VI. This discrepancy between measured and expected f_0 and R_{eff} may be attributed to the prototype resonator volume which is slightly larger than 1 cm^3 , and current crowding at the edges of the capacitor plates. Experimentally, this current crowding can be reduced by adding blocks of low-loss magnetic cores at the ends of the resonator to straighten magnetic field lines. We tested this using blocks of Fair-Rite 67 material, which resulted in $R_{epr} = 1.76 \Omega$, $R_{esr} = 0.45 \text{ m}\Omega$ and $R_{eff} = 2.22 \text{ m}\Omega$ at 2.40 MHz (Fig. 10, Table VI). This R_{eff} with magnetic cores is closer to the predicted R_{eff} , verifying the effect of current crowding. The measured R_{eff} of the prototype LC resonator matches closely with the calculated R_{eff} represented by “C0G practical” curve in Fig. 10. This verifies the R_{eff} model of the LC resonator presented in Section IV-B.

C. Large-Signal Test

A large-signal test was performed to measure the ac voltage capability of the implemented parallel resonator. This ac voltage capability can be used to compute the ac current capability of the corresponding series resonator, which in turn can be used to calculate the output power of a ReSC resonator using this series resonator. The parallel resonator, rather than the series resonator, was used in this large-signal test because of the difficulty of matching a 50Ω output impedance of a power amplifier to the very low $0.56 \text{ m}\Omega$ R_{esr} of the series resonator; the higher 1.13Ω R_{epr} of the parallel resonator is more easily matched to a 50Ω impedance. In order to obtain a more conservative estimate of the power handling capability of the resonator, the large-signal test was performed without using the magnetic cores to straighten the field lines and reduce losses.

The measurement setup (Fig. 12 (a)) includes a 50Ω to 3Ω AVTECH AVX-M4 matching transformer, a Pearson 6585 current transformer and an Agilent 1141A differential voltage probe. The measurement setup is based on the configuration detailed in [49]. A sinusoidal voltage signal from a function generator was amplified by a Tomco BT00500-AlphaS-CW power amplifier and fed into the matching transformer. The voltage across and the current through the parallel resonator (V_p and I_p) were measured using the differential voltage probe and the current transformer respectively. The frequency was tuned to resonance, and at resonance, the power loss in the resonator was calculated from the product of the rms values of these waveforms. The maximum surface temperature T_{max} of the resonator was measured using a FLIR E60 thermal camera. Fig. 12 (b) shows the temperature profile of the parallel

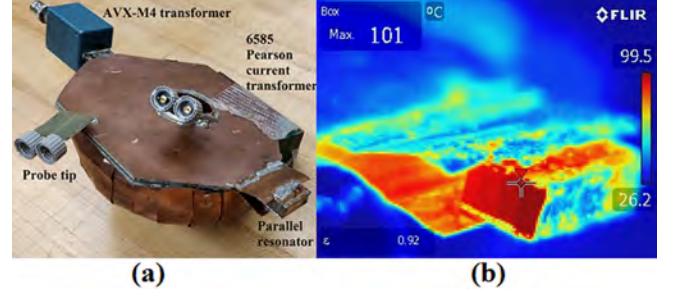


Fig. 12. The large-signal measurement. (a) The measurement setup showing the impedance matching transformer, current monitor, the voltage probe points and the parallel resonator. (b) Temperature profile of the parallel resonator operating around 100 °C.

resonator operating near the maximum allowable temperature, measured using the thermal camera.

The drive level was gradually increased until the maximum steady-state surface temperature was around 100 °C. Considering the temperature difference between the surface and the inner hotspot, higher drive levels would push the capacitors above the rated temperature of 125 °C. The drive frequency had to be adjusted for each drive level and temperature so that the measured voltage and current waveforms are in phase, indicating that the resonator is operating at resonance. The resonance frequency varied from 2.73 MHz at room temperature to 2.64 MHz at 101 °C maximum steady-state surface temperature. This variation in the resonance frequency is due to the dependence of the dielectric permittivity, hence the capacitance, on the temperature and the drive level.

The impedance at resonance R_{epr} of the parallel resonator was calculated by $R_{epr} = V_{p,rms}/I_{p,rms}$. The ESR of the corresponding series resonator R_{esr} was then calculated using R_{epr} , the drive frequency and the inductance measured in the small signal test. The measured R_{epr} and the corresponding calculated R_{esr} are plotted as a function of the measured maximum surface temperature in Fig. 13. These measured resistances at room temperature agree with the small signal test results. At higher drive levels, the higher loss in the resonator increases the temperature, which results in a lower R_{epr} and a higher R_{esr} as shown in Fig. 13. This indicates that the small signal R_{epr} and R_{esr} accurately represent the resonator loss at room temperature but high-temperature effects may need to be considered for a more accurate loss model. However, because the difference between the resistances at 100 °C and that at the room temperature is only 21%, the presented loss model can be considered sufficient in the order-of-magnitude analysis intended for this paper.

The measured rms voltage of the parallel resonator $V_{p,rms}$ can be used to calculate the rms current through the corresponding series resonator $I_{s,rms}$ by equating the energy stored in the two resonators $CV_{p,rms}^2 = LI_{s,rms}^2$. Fig. 14 shows $V_{p,rms}$ and $I_{s,rms}$ as a function of the measured temperature; $I_{s,rms}$ can be as high as 82.4 A for operation at 101 °C with 25 °C ambient temperature. This 82.4 A I_{rms} with $0.67 \text{ m}\Omega$ R_{esr} gives a total loss of 4.56 W, resulting in a loss per unit surface area of 0.6 W/cm^2 . This is lower than the 3 W/cm^2 tolerable loss limit used in Section II-C to

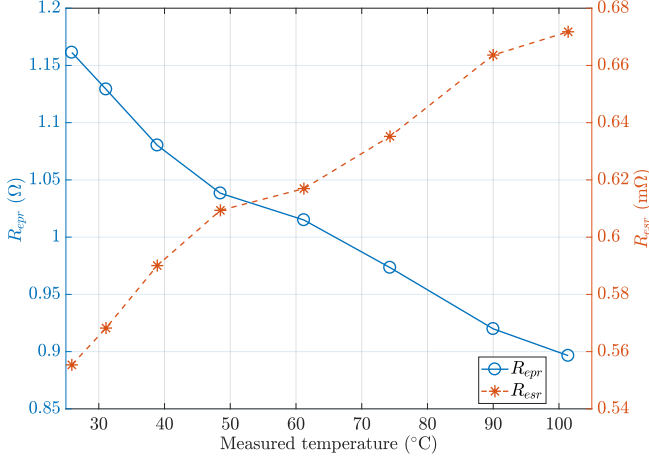


Fig. 13. Measured impedance at resonance of the parallel resonator and the corresponding series resonator impedance vs. measured maximum steady-state surface temperature.

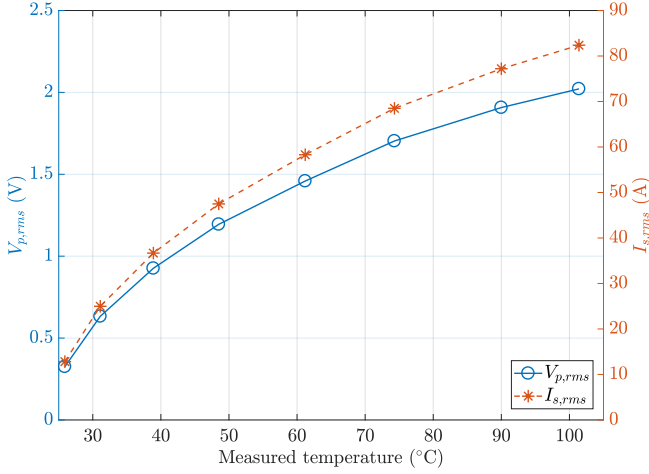


Fig. 14. Measured rms voltage of the parallel resonator and the rms current of the corresponding series resonator vs. measured maximum steady-state surface temperature.

calculate the energy density of inductors and in Section V-B to compare the power throughput of the piezoelectric and LC resonators. However, the 3 W/cm^2 limit was used as an upper limit for loss calculation and a standard for comparing different resonators rather than as an expected loss; the actual tolerable loss limit depends on the thermal resistance and the mechanical design of each resonator.

Consider the application of this resonator in a simple 1:1 ReSC converter. With the 250 V rated capacitors operated at 200 V, the input and output voltages of the converter are also 200 V. Although switching losses in presently available power devices are likely to be problematic at this voltage and frequency, we assume ideal switch operation in order to address the capability of the passive component independent of available semiconductors. Based on the rms current capability $I_{s,rms}$, we calculate the dc output current of the ReSC converter using the series resonator by equating $I_{s,rms}^2 R_{esr} = I_{dc}^2 R_{eff}$ [27], resulting in $I_{dc} = \sqrt{2} I_{s,rms} / \pi$; the 82.4 A $I_{s,rms}$ results in $I_{dc} = 37.1 \text{ A}$. This output voltage and I_{dc}

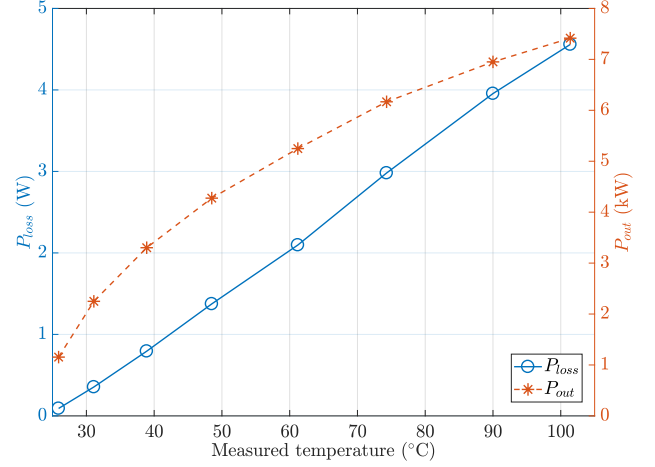


Fig. 15. Measured power loss of the parallel resonator and the power throughput of a ReSC converter using the corresponding series resonator vs. measured maximum steady-state surface temperature.

can be used to calculate the power capability of the ReSC converter; Fig. 15 shows the ReSC converter power output as well as the corresponding power loss. At high temperatures, the increase in P_{out} is smaller because the resonator ESR increases with the temperature.

It can be seen from Fig. 15 that the presented resonator can handle a power as high as 7.42 kW with a power loss of only 4.56 W (0.06% loss) attributable to the resonator. This result is specific to operation at 101 °C with an ambient temperature of 25 °C and operation in a higher ambient temperature will decrease the resonator power capability. However, given that the resonator only has a 1.14 cm^3 volume, it can be concluded that the power switches and interconnects, rather than the passive components, limit the performance of a ReSC converter using this prototype resonator.

VII. CONCLUSION

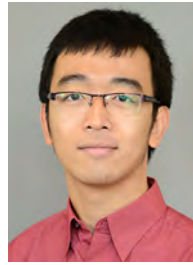
We have presented a fundamental analysis of various energy storage mechanisms and a possible power circuit for using mass-spring resonance in power converters. Mechanical energy storage is explored as an alternative to LC resonant tanks because it provides at least an order of magnitude higher energy density than the electrical alternatives. A comparison of the two types of resonance in the ideal scenarios show that the piezoelectric resonator is more efficient overall and provides a higher power output than LC resonators with skin effect. However, when used in a resonant switched-capacitor type circuit, both resonators are capable of very low effective resistances and high power handling capabilities in the kW range in a 1 cm^3 volume, much higher than the capabilities of the current passive component technology. The low effective resistance of LC resonators was also verified with a prototype resonator which has a low $2.4 \text{ m}\Omega$ output impedance at resonance. A large-signal test shows that the resonator is capable of handling 7.42 kW with only 0.06% loss attributable to the resonator with a maximum surface temperature of 101 °C in an ambient temperature of 25 °C.

To examine the future potential, our analysis deliberately omitted practical constraints of today's technology. This analysis allowed us to eliminate many technologies, but it shows that both piezoelectric and electromagnetic resonators may have the potential to offer much higher efficiency and power than do typical passive components in use today. The choice between these two favored technologies is likely to hinge on the factors that have been ignored or idealized in this analysis. For the piezoelectric resonator, such factors include the specific vibration modes, the mounting type and position, the poling electrodes and the multilayer structure. For the LC resonator, factors such as the dielectric loss and the core loss need to be considered. Because our analysis used high performance materials, namely lithium niobate and alkali-free glass dielectric, commercial development of these materials is also important for realizing the high performance discussed in this paper. The difference between a ReSC-type circuit and a series resonant converter, and hence the effect of circuit design, also needs to be explored. The effects of all of these factors are important topics for future research.

REFERENCES

- [1] C. R. Sullivan, D. Yao, G. Gamache, A. Latham, and J. Qiu, "(Invited) Passive component technologies for advanced power conversion enabled by wide-band-gap power devices," *ECS Transactions*, vol. 41, no. 8, pp. 315–330, 2011.
- [2] J. W. Kolar, D. Bortis, and D. Neumayr, "The ideal switch is not enough," in *Power Semiconductor Devices and ICs (ISPSD), 28th International Symposium on*. IEEE, 2016, pp. 15–22.
- [3] D. J. Perreault, J. Hu, J. M. Rivas, Y. Han, O. Leitermann, R. C. N. Pilawa-Podgurski, A. Sagneri, and C. R. Sullivan, "Opportunities and challenges in very high frequency power conversion," in *24th Annual IEEE Applied Power Electronics Conference and Exposition (APEC)*, 2009, pp. 1–14.
- [4] C. Ó. Mathúna, N. Wang, S. Kulkarni, and S. Roy, "Review of integrated magnetics for power supply on chip (PwrSoC)," *IEEE Transactions on Power Electronics*, vol. 27, no. 11, pp. 4799–4816, 2012.
- [5] J. M. Noworolski and S. R. Sanders, "An electrostatic microresonant power conversion device," in *23rd Annual IEEE Power Electronics Specialists Conference (PESC)*. IEEE, 1992, pp. 997–1002.
- [6] C. A. Rosen, "Analysis and design of ceramic transformers and filter elements," Ph.D. dissertation, Syracuse University, 1956.
- [7] Y. Fuda, K. Kumasaka, M. Katsuno, H. Sato, and Y. Ino, "Piezoelectric transformer for cold cathode fluorescent lamp inverter," *Japanese Journal of Applied Physics*, vol. 36, no. 5S, pp. 3050–3052, 1997.
- [8] J. Yoo, K. Yoon, S. Hwang, S. Suh, J. Kim, and C. Yoo, "Electrical characteristics of high power piezoelectric transformer for 28 W fluorescent lamp," *Sensors and Actuators A: Physical*, vol. 90, no. 1, pp. 132–137, 2001.
- [9] T. Zaitzu, Y. Fuda, Y. Okabe, T. Ninomiya, S. Hamamura, and M. Katsuno, "New piezoelectric transformer converter for ac-adaptor," in *Twelfth Annual Applied Power Electronics Conference and Exposition (APEC)*, vol. 2. IEEE, 1997, pp. 568–572.
- [10] O. Ohnishi, Y. Sasaki, T. Zaitzu, H. Kishie, and T. Inoue, "Piezoelectric ceramic transformer for power supply operating in thickness extensional vibration mode," *IEICE transactions on fundamentals of electronics, communications and computer sciences*, vol. 77, no. 12, pp. 2098–2105, 1994.
- [11] P. A. Kyaw and C. R. Sullivan, "Fundamental examination of multiple potential passive component technologies for future power electronics," in *IEEE 16th Workshop on Control and Modeling for Power Electronics (COMPEL)*, 2015.
- [12] P. A. Kyaw, A. L. F. Stein, and C. R. Sullivan, "Optimizing resonant tanks for high power density using standard capacitors," in *IEEE 18th Workshop on Control and Modeling for Power Electronics*, 2017.
- [13] M. F. Ashby, *Materials selection in mechanical design*, 4th ed. Burlington, MA: Butterworth-Heinemann, 2011.
- [14] N. J. Smith, B. Rangarajan, M. T. Lanagan, and C. G. Pantano, "Alkali-free glass as a high energy density dielectric material," *Materials Letters*, vol. 63, no. 15, pp. 1245–1248, 2009.
- [15] Q. Li, K. Han, M. R. Gadinski, G. Zhang, and Q. Wang, "High energy and power density capacitors from solution-processed ternary ferroelectric polymer nanocomposites," *Advanced Materials*, vol. 25, no. 36, pp. 6244–6249, 2014.
- [16] W. Li, L. Jiang, X. Zhang, Y. Shen, and C. Nan, "High-energy-density dielectric films based on polyvinylidene fluoride and aromatic polythiourea for capacitors," *Journal of Materials Chemistry A*, vol. 2, no. 38, pp. 15 803–15 807, 2014.
- [17] C. Liu, Z. Yu, D. Neff, A. Zhamu, and B. Z. Jang, "Graphene-based supercapacitor with an ultrahigh energy density," *Nano Letters*, vol. 10, no. 12, pp. 4863–4868, 2010.
- [18] A. Yu, V. Chabot, and J. Zhang, *Electrochemical supercapacitors for energy storage and delivery: fundamentals and applications*. CRC Press, 2013.
- [19] H. Bluhm, *Pulsed Power Systems: Principles and Applications*. Berlin: Springer, 2006.
- [20] Digi-Key Electronics. Online catalog for surface mount resistors. [Online]. Available: <http://www.digikey.com/product-search/en/resistors/chip-resistor-surface-mount/65769> Accessed on: Oct. 27, 2015.
- [21] M. E. Dale and C. R. Sullivan, "General comparison of power loss in single-layer and multi-layer windings," in *IEEE 36th Power Electronics Specialists Conference (PESC)*. IEEE, 2005, pp. 582–589.
- [22] C. R. Sullivan, D. V. Harburg, J. Qiu, C. G. Levey, and D. Yao, "Integrating magnetics for on-chip power: A perspective," *IEEE Transactions on Power Electronics*, vol. 28, no. 9, pp. 4342–4353, 2013.
- [23] K. Uchino, "Piezoelectric ultrasonic motors: overview," *Smart Materials and Structures*, vol. 7, no. 3, p. 273, 1998.
- [24] B. Koc, S. Catay, and K. Uchino, "A piezoelectric motor using two orthogonal bending modes of a hollow cylinder," *IEEE Transactions on Ultrasonics, Ferroelectrics and Frequency Control*, vol. 49, no. 4, pp. 495–500, 2002.
- [25] Y. Liu, W. Chen, P. Feng, and J. Liu, "A rotary piezoelectric motor using bending vibrators," *Sensors and Actuators A: Physical*, vol. 196, pp. 48–54, 2013.
- [26] M. Shoyama, T. Naka, and T. Ninomiya, "Resonant switched capacitor converter with high efficiency," in *IEEE 35th Annual Power Electronics Specialists Conference (PESC)*, vol. 5. IEEE, 2004, pp. 3780–3786.
- [27] K. Kesarwani and J. T. Stauth, "A comparative theoretical analysis of distributed ladder converters for sub-module PV energy optimization," in *IEEE 13th Workshop on Control and Modeling for Power Electronics (COMPEL)*, 2012, pp. 1–6.
- [28] K. S. Van Dyke, "The piezo-electric resonator and its equivalent network," *Proceedings of the Institute of Radio Engineers*, vol. 16, no. 6, pp. 742–764, 1928.
- [29] M. Pijolat, A. Reinhardt, E. Defay, C. Deguet, D. Mercier, M. Aid, J. S. Moulet, B. Ghyseln, D. Gachon, and S. Ballandras, "Large Qxf product for HBAR using smart cut™ transfer of LiNbO₃ thin layers onto LiNbO₃ substrate," in *IEEE Ultrasonic Symposium (IUS)*. IEEE, 2008, pp. 201–204.
- [30] S. A. Chandorkar, M. Agarwal, R. Melamud, R. N. Candler, K. E. Goodson, and T. W. Kenny, "Limits of quality factor in bulk-mode micromechanical resonators," in *IEEE 21st International Conference on Micro Electro Mechanical Systems (MEMS)*. IEEE, 2008, pp. 74–77.
- [31] S. Gong and G. Piazza, "Design and analysis of lithium-niobate-based high electromechanical coupling RF-MEMS resonators for wideband filtering," *IEEE Transactions on Microwave Theory and Techniques*, vol. 61, no. 1, pp. 403–414, 2013.
- [32] Boston Piezo Optics Inc. Lithium niobate physical properties. [Online]. Available: <http://www.bostonpiezooptics.com/lithium-niobate> Accessed on: Mar 25, 2015.
- [33] A. Rivera, G. Garcia, J. Olivares, M. L. Crespillo, and F. Agulló-López, "Elastic (stress-strain) halo associated with ion-induced nano-tracks in lithium niobate: role of crystal anisotropy," *Journal of Physics D: Applied Physics*, vol. 44, no. 47, p. 475301, 2011.
- [34] M.-J. Jin, O.-Y. Jeon, B.-J. Kim, and M. Cha, "Fabrication of periodically poled lithium niobate crystal and poling-quality evaluation by diffraction measurement," *Journal of the Korean Physical Society*, vol. 47, pp. S336–S339, 2005.
- [35] M. Domenjoud, M. Lematre, M. Gratton, M. Lethiecq, and L.-P. Tran-Huu-Hue, "Theoretical and experimental study of the electroacoustic behavior of lithium niobate under an initial mechanical stress," *IEEE Transactions on Ultrasonics, Ferroelectrics and Frequency Control*, vol. 60, no. 10, pp. 2219–2224, 2013.
- [36] C. Schaefer and J. T. Stauth, "A 3-phase resonant switched capacitor converter delivering 7.7 W at 85% efficiency using 1.1 nH PCB trace inductors," *IEEE Journal of Solid-State Circuits*, vol. 50, no. 12, pp. 2861–2869, 2015.

- [37] S. Pasternak, C. Schaefer, and J. Stauth, "Equivalent resistance approach to optimization, analysis and comparison of hybrid/resonant switched-capacitor converters," in *Control and Modeling for Power Electronics (COMPEL)*, IEEE 17th Workshop on, 2016, pp. 1–8.
- [38] A. Blumenfeld, A. Cervera, and M. M. Peretz, "Enhanced differential power processor for pv systems: Resonant switched-capacitor gyrator converter with local mppt," *IEEE Journal of Emerging and Selected Topics in Power Electronics*, vol. 2, no. 4, pp. 883–892, 2014.
- [39] K. Kesarwani and J. T. Stauth, "Resonant and multi-mode operation of flying capacitor multi-level dc-dc converters," in *Control and Modeling for Power Electronics (COMPEL)*, IEEE 16th Workshop on, 2015, pp. 1–8.
- [40] Y. Li, J. Chen, M. John, R. Liou, and S. R. Sanders, "Resonant switched capacitor stacked topology enabling high dc-dc voltage conversion ratios and efficient wide range regulation," in *Energy Conversion Congress and Exposition (ECCE)*, IEEE, 2016.
- [41] Digi-Key Electronics. Online catalog for surface mount ceramic capacitors. [Online]. Available: <http://www.digikey.com/products/en/capacitors/ceramic-capacitors/60> Accessed on: Mar 06, 2017.
- [42] TDK. (2015) SEAT 2013 - Selection Assistant of TDK components. [Online]. Available: <https://product.tdk.com/info/en/technicalsupport/seat/index.html> Accessed on: Feb 06, 2017.
- [43] AVX. (2015) Spicap 3.0. [Online]. Available: <http://www.avx.com/resources/design-tools/> Accessed on: Oct. 03, 2015.
- [44] Kemet. K-sim (webspice). [Online]. Available: <http://ksim.kemet.com/Ceramic/CeramicCapSelection.aspx> Accessed on: Nov 08, 2016.
- [45] "Radio instruments and measurements," *Bureau of Standards Circular*, vol. C74, p. 252, January 1937.
- [46] S. Chen. Particle swarm toolbox for MATLAB. [Online]. Available: <https://code.google.com/p/psomatlabs/> Accessed on: Feb 19, 2015.
- [47] J. B. Fedison, M. Fornage, M. J. Harrison, and D. R. Zimmanck, " C_{oss} related energy loss in power MOSFETs used in zero-voltage-switched applications," in *Applied Power Electronics Conference and Exposition (APEC)*, Twenty-Ninth Annual IEEE, 2014, pp. 150–156.
- [48] V. Kaajakari, T. Mattila, A. Oja, and H. Seppä, "Nonlinear limits for single-crystal silicon microresonators," *Journal of Microelectromechanical Systems*, vol. 13, no. 5, pp. 715–724, 2004.
- [49] H. Syed and C. R. Sullivan, "High frequency magnetic toroidal core loss measurement fixture," in *28th Annual IEEE Applied Power Electronics Conference and Exposition (APEC)*, 2013, pp. 2466–2473.



Phyoo Aung Kyaw (S'15) received the B.A. degree in physics from the Amherst College, Amherst, MA, USA, in 2014. He is currently working towards his Ph.D. degree in electrical engineering at Dartmouth College, Hanover, NH, USA. His research interests include power electronics and magnetics, electromagnetic and piezoelectric resonators, high-frequency passive components, and wireless power transfer.



Aaron L.F. Stein received the Ph.D. degree in electrical engineering and computer science from the University of Michigan, Ann Arbor, MI, USA, in 2016, and is currently a Post-Doctoral Research Associate at Dartmouth College, Hanover, NH, USA. He has published technical papers on topics including wireless power transfer, energy harvesting, and electromagnetic components.



Charles R. Sullivan (S'93-M'96-SM'12-F'14) received the B.S.(Hons.) degree in electrical engineering from Princeton University, Princeton, NJ, USA, in 1987, and the Ph.D. degree in electrical engineering from the University of California, Berkeley, CA, USA, in 1996.

Between the B.S. and Ph.D. degrees, he was with Lutron Electronics designing electronic ballasts. He is currently a Professor at Thayer School of Engineering at Dartmouth, Hanover, NH, USA.

His research interests include design optimization of magnetics for power applications, energy efficiency, and renewable energy, and electromagnetic modeling of capacitors.

Dr. Sullivan received the National Science Foundation CAREER Award and two Power Electronic Society Prize Paper Awards.